

We are IntechOpen, the world's leading publisher of Open Access books Built by scientists, for scientists

6,900

Open access books available

185,000

International authors and editors

200M

Downloads

Our authors are among the

154

Countries delivered to

TOP 1%

most cited scientists

12.2%

Contributors from top 500 universities



WEB OF SCIENCE™

Selection of our books indexed in the Book Citation Index
in Web of Science™ Core Collection (BKCI)

Interested in publishing with us?
Contact book.department@intechopen.com

Numbers displayed above are based on latest data collected.
For more information visit www.intechopen.com



Near-Field Propagation Analysis for Traveling-Wave Antennas

Ha Hoang

Abstract

The evolution of ElectroMagnetic (EM) models and modern EM solvers permit resolving a variety of real-life EM propagation and radiation problems, in which antenna design and optimization account a large proportion. However, understanding of EM propagation processes on antenna structures and design achievements can be limited when only total antenna responses are considered and there is lacking of near-field analysis. This chapter provides a better insight into the EM propagation processes on traveling-wave antennas. A near-field propagation analysis method is proposed based on simulated near-field data with corresponding meshed structure data. This overcomes the insufficiencies and obstacles for observation of the conventional analysis methods. The EM-solver-run optimization and accurate sampling for field and structure data are the first important steps for the analysis. For general propagation problems such as paths recognition and characterization of the propagation, the EM signal models, impulse response analysis and super-resolution algorithms for Time of Arrival (ToA) estimation are studied and proposed. A particular space/time/frequency analysis is implemented for traveling-wave Vivaldi antennas, in which the phenomenon of EM energy transfer out of the conducting elements into the free space and higher-order scattering processes are revealed. The refined adjustment and optimization for the antennas are also proposed.

Keywords: near-field propagation, radiating propagating process, traveling-wave antennas, impulse response analysis, MUSIC algorithm, electromagnetic simulation, electromagnetic modeling

1. Introduction

The concepts of traveling wave and standing wave can be used to categorize antenna types with corresponding dominant propagation mode for radiating. Traveling-wave antennas [1] often have long electrical length in the main propagation path, and the EM energy radiating proportion prevails over the reflected proportion in the propagation along the main path. In contrast, in standing-wave antennas, the EM energy reflects many times in the main propagation path. This causes the standing-wave or resonance phenomena and increases the EM field intensities with appropriate periodic excitation source, and this facilitates to increase the radiating proportion for a certain bandwidth (BW). The standing-wave antennas often have high Q-factor and with narrow BW, while these characteristics are opposite for the traveling-wave antennas. However, this categorization for the antennas is relative because the propagation mode for radiating depends on the

actual structure and is only dominant over a certain band of frequencies. Traveling-wave antennas have been the research subject of many reports, and Vivaldi antennas [2] are the typical branch of traveling-wave antennas.

To model EM fields, characterize structural/operational features and optimize the performances for traveling-wave antennas, various approaches have been implemented. Transverse EM (TEM)-mode transmission line models have been used to describe the propagating and radiating mechanism of these antennas. For example, stepped-width transmission line slots connected end to end were used for the Vivaldi antenna, and the effect of the stepped discontinuities was solved by a power continuity criterion in [3], and in [4], a design process with least-square optimization was implemented for the calculation of input impedance and power division at the junctions of a stepped line by a transmission matrix chain. However, simplicity of the models constrained the accuracy and practical application of such methods.

Model accuracy improvements based on approximation to the conical slot lines [5, 6] yield electric field distributions and radiating fields with Green's functions. Diffraction at the end of the radiating slot and lateral edges was incorporated by a weight pattern for each edge. These improvements achieved the better predictions than the TEM-mode transmission line models.

While, in general, the EM propagation knowledge in a specific antenna structure is required for modeling, numerical three-dimensional EM solvers segment and discrete a structural space into a meshed volume of cells adapted to the material and geometric properties of the structure. Space, time and/or frequency distributions of EM energy in the volume are established, *a priori*, by solving Maxwell's equations numerically or approximately on a cell-by-cell basis for overall volume while taking account the boundary and excitation conditions. These EM distributions are the basic for derived total or global antenna characteristics, for example scattering parameters, far-field response.

Parallel improvements in EM wave theory, material characterization, numerical techniques, fast algorithms, and high-performance computing have realized faster, more accurate EM solvers for highly complex and real-life problems [7]. The improvements have even supported the design of complicated antipodal Vivaldi antennas from fractal fern leaf-shaped geometries [8]. By using EM solvers with feasible processes for design optimization, a variety of traveling-wave antennas with diverse EM responses have been proposed. Optimization of the conventional geometry and modifications/additions are the common methods to attain improved antenna performances such as in [9–12]. To explain the complex EM characteristics of the antenna geometries and the effects from the added elements in [10–12], direct observations of EM near-field vectors and of metal surface currents were implemented.

In a new near-field propagation research, an analysis method for the propagation of distributed near fields from a full-wave EM solver for the typical traveling-wave antenna has been proposed [13]. With an adequately accurate data set of near field in the time and/or frequency domains for the antenna structure corresponding to a excitation condition, the EM fields in key regions can be evaluated and quantified to expose the relationships between the geometric properties and space, time and/or frequency EM energy distributions. The correlation characteristics reveal causal relationships of the geometric properties to the EM field propagation process.

Because the EM fields on the specific regions of the structure were observed and analysed based on time-domain impulse response analysis, the results were not be affected by superpositions of excited periodic cycles such as the conventional frequency-analysis method, it revealed the propagation processes of EM energy clusters and geometry-property influence details on the structure. Moreover, observations of EM responses at a consecutive point set along the dominant EM energy flows were implemented to analyse propagation progresses and the

scattering components between the sections in the structure. This avoided locality in observation and permitted to overcome analysis bandwidth limits. Super-resolution algorithms such as MULTiple Signal Classification (MUSIC) were also useful [14] to tackle these limits.

The rendered details in the space, time and/or frequency of the results are a powerful feature of the analysis method for the antenna design. The quantitative and qualitative analyses can be implemented to characterize for a subpart of the time and/or frequency EM energy response at each position in space and propagation mechanism dependency on a particular part of the structure. Design and optimization methods, built on such analysis, respond for refined adjustment of the structures. This approach reveals a new, deeper perspective in the hierarchy of antenna and related system design.

2. Near-field propagation analysis methods

2.1 Data sampling from time-domain EM solver

In this method, CST Microwave Studio (MWS) is used as the EM solver in the time domain. Structural, mesh and near-field vector data are extracted for the near-field propagation analysis process. This section presents the features of these data as well as sampling problems and their solutions.

2.1.1 Structure data sampling

The hexahedral meshing algorithm is used within time-domain MWS solver to generate mesh cells adapted to material and geometric properties to represent the input structure and background space. MWS solves and establishes the near-field distributions on this meshed representation rather than the input structure. Structures such as Vivaldi antennas contain diagonal components in the Vivaldi-curved edges that are not parallel with any of the coordinate axes. This causes a stepped or staircase mesh structure to represent these structural components.

The algorithm in the structural data sampling step extracts the meshing lines and the material matrix data of the whole simulation space from the MWS solver, and it reconstructs the meshed structure of the main elements of the structure for the next sampling and analysis steps. Specifically, based on the material matrix data, the metal cells of the meshed metal patches of the Vivaldi antenna are identified. These cells are merged together into a reconstructed structure of the meshed metal patch. **Figure 1** shows the top surface of a small piece of the reconstructed metal patch with the staircase meshed structure for the Vivaldi edge. The reconstructed structure becomes basic for the field data sampling step.

2.1.2 Near-field vector data sampling

The complexity and size of an EM simulation are governed by the detail and size of the structure and surrounding space, and the frequency band of interest. These simulating features affect the number of mesh cells and the time step of the EM solving. To achieve high spatial resolution for the analysis, the excitation signal BW must be adequate, and it can be larger than the operational BW of the antenna. To guarantee convergence condition, the time step can be much smaller than the time step corresponding to the excitation signal Nyquist BW. Therefore, it does not need to sample all the computed near-field data in the simulating time. The duration of the EM solving depends on the volume of the simulation space, degree of EM energy

Parameters	Values
Simulation space volume	$84 \times 40 \times 10.267 \text{ mm}^3$
Simulation BW	0 – 80 GHz
Number of mesh cells	11, 269, 952
Time duration	1.25 ns
Sampling time step	1 ps
Total size of EM near-field data	320 GB

Table 1.
EM solving and sampling parameters of a simulation example.

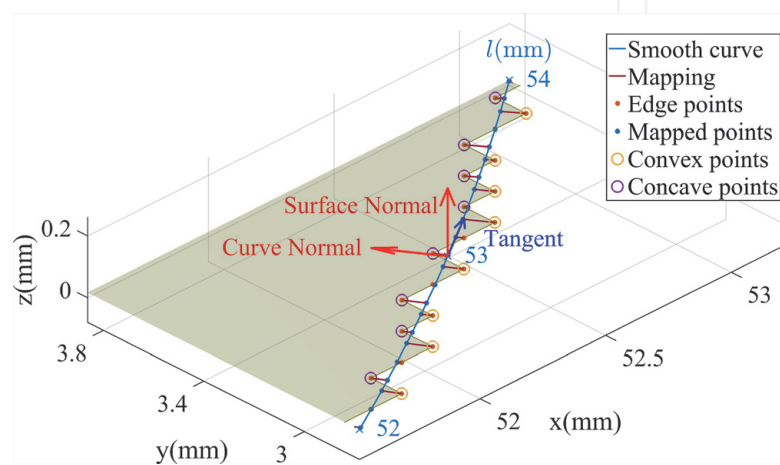


Figure 1.
Reconstructed structure and mapping of the Vivaldi edge points to the smooth polynomial curve.

stored in the structure, the length of the excitation signal and accuracy requirement of the analysis, especially for low-frequency or long-delay-time components.

An example of EM solving and sampling parameters for a Vivaldi antenna structure is presented in **Table 1**. EM field vector data are sampled in the simulating space and time. Each vector is represented by three scalar components. With single-precision floating point format, each scalar component uses 32 bits in size. The total size of the sampled EM near-field data can reach hundreds of gigabytes.

The Vivaldi edges are the main parts of this traveling-wave antenna structure, and a significant proportion of EM energy concentrates along these edges. Space, time and frequency distributions of the EM fields along these edges contain the most important information about the EM energy propagation; therefore, accurate sampling of field data in these regions is essential.

The sampling is based on fitting a nine-order polynomial smooth curve on the stepped structure of the reconstructed structure from the meshed structure, as shown **Figure 1**. As expected, this curve represents the Vivaldi curve of the input structure, at which there is a transition in material property from conductor to dielectric/vacuum. Therefore, there is also a corresponding transition in the field vectors at the edge. To preserve this attribute in the sampled data, the EM field vectors at the edge points of the reconstructed structure are mapped to the nearest points on the smooth curve, and these represent the field vectors on the Vivaldi edge of the input structure. The tangential and normal vector components of the EM field vectors can also be divided from the sampled vectors as shown in **Figure 1**. A three-dimensional interpolation from the field vector data at mesh cell vertices

around the mapped point is also a method for the sampling. However, because of the dependence of interpolated result on distance to the mapped point and the difference between field vectors inside the conducting patch and field vectors at the edge of the patch (especially in the vector direction), there can be a significant error in the interpolation result if a mapped point closes to a mesh cell vertex inside the conducting patch.

The field vector data for the lateral and end edges of the conducting patches are sampled by extracting the vector data directly on mesh cell vertices corresponding to these edges. The field vector data at positions in dielectric/vacuum volumes are sampled by interpolated data from the nearest mesh cell vertices.

2.2 Time- and frequency-domain-based analysis methods

2.2.1 Impulse response analysis

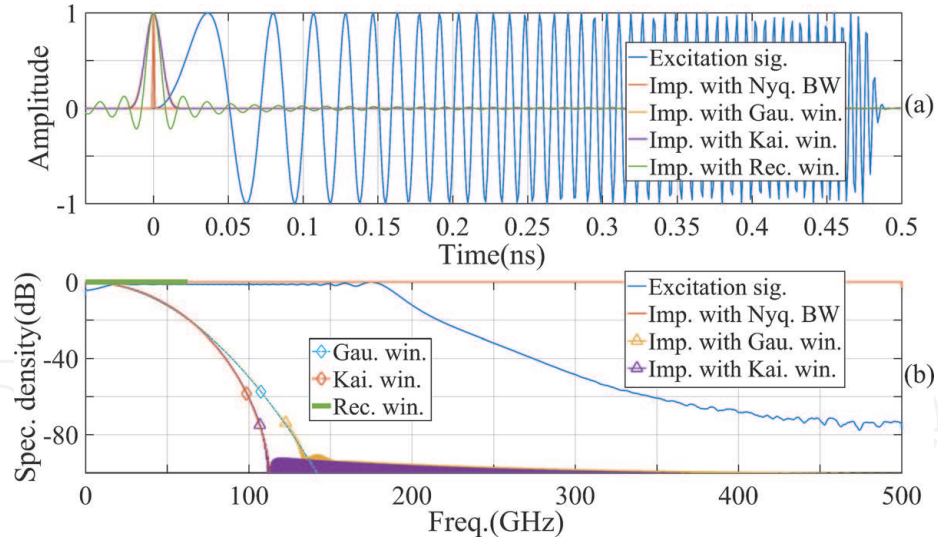
With the time-domain-based method (TDbM), the analysis is started by an EM simulation with an impulse excitation signal (e.g., Gaussian signal) covering a certain analysis BW. The observed signals are directly extracted from the EM-simulating data. The EM responses on the structure can be analyzed directly in the time domain or can be transformed to the frequency domain by the discrete Fourier transform (DFT). An ineffectiveness of the analysis method is that the EM solver must be rerun whenever there is a change in the analysis BW, and the frequency-domain-based method (FDbM) is a solution proposed to improve the analysis performance.

By the FDbM, the EM solver was only run once with an excitation signal covering a wide enough BW of all analysis sub-bandwidth segments. Then, transformations to the frequency domain for the excitation signal and the observed signals are implemented based on DFT. To compensate the unequal in magnitude and phase of the frequency components of the excitation signal, an equalization is implemented for the frequency components of the observed signals.

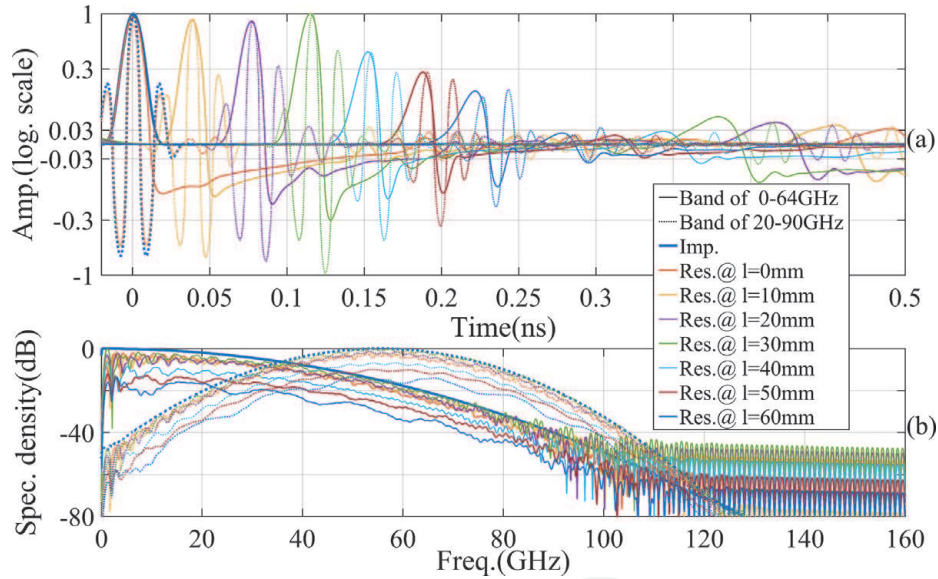
Then, the compensated observed signals are transformed into the time domain by inverse DFT. Thus, when the excitation signal is processed and transformed to the time domain, all of its frequency components are equal in magnitude and phase; it is a full Nyquist BW impulse signal. The compensated observed signals in time domain are the responses of this impulse. However, in practical, the compensation can gain noise levels excessively for low-energy-level frequency components for an observed signal with a certain signal-to-noise ratio (SNR), especially at the upper end of the simulating band. Therefore, the responses with full Nyquist BW cannot be achieved in practice. Rectangular, Gaussian and Kaiser windows are used to limit the analysis sub-bandwidth segments in this work.

A frequency-modulated continuous wave (FMCW) is chosen for the excitation signal. This linear chirp sweeps from 0 to 180 GHz in 0.5 ns and covering a BW of 0–210 GHz. **Figure 2** shows this excitation signal and the impulse signals corresponding to the different windows in the time and frequency domains. The impulses and responses in **Figure 3** are the result of process using a Gaussian window in a low-pass analysis band of 0–64 GHz and a band-pass analysis band of 20–90 GHz (–20 dB BW is standard) in the time and frequency domains. The response signals are curve normal vector component of the E-field at points along a Vivaldi edge located a distance l from the excitation source as shown by the smooth curve in **Figure 1**.

The differences between the TDbM and the FDbM results are also examined. For TDbM, the EM simulation uses a Gaussian impulse excitation signal with a BW of 0–64 GHz in time domain. For FDbM, the EM simulation uses an FMCW excitation signal with a BW of 0–210 GHz in time domain, and a Gaussian window

**Figure 2.**

The FMCW excitation signal and FDbM impulse signals with different windows in the (a) time and (b) frequency domains.

**Figure 3.**

The FDbM impulse signal and responses in the (a) time and (b) frequency domains at the points along the Vivaldi edge.

with a low-pass BW of 0–64 GHz is used in the analysis frequency limitation. The impulse signal pair, the response pairs, and their errors are shown in **Figure 4**. These comparisons demonstrate a good agreement between the TDbM and FDbM.

2.2.2 MUSIC algorithm for ToA estimation

As a well-known super-resolution algorithm, MUSIC is often used for signal analysis [15, 16], especially in cases of the overlap of many signals and/or limitation in analysis BW. The MUSIC algorithm is applied in this work for ToA or time delay estimation of dominant components/clusters in the observed signals.

The signal applied at the antenna excitation port is $x(t)$. Because of multiple overlapping EM energy flows propagating along different paths in the structure, the observed signal at an arbitrary position in the simulating space is considered as a

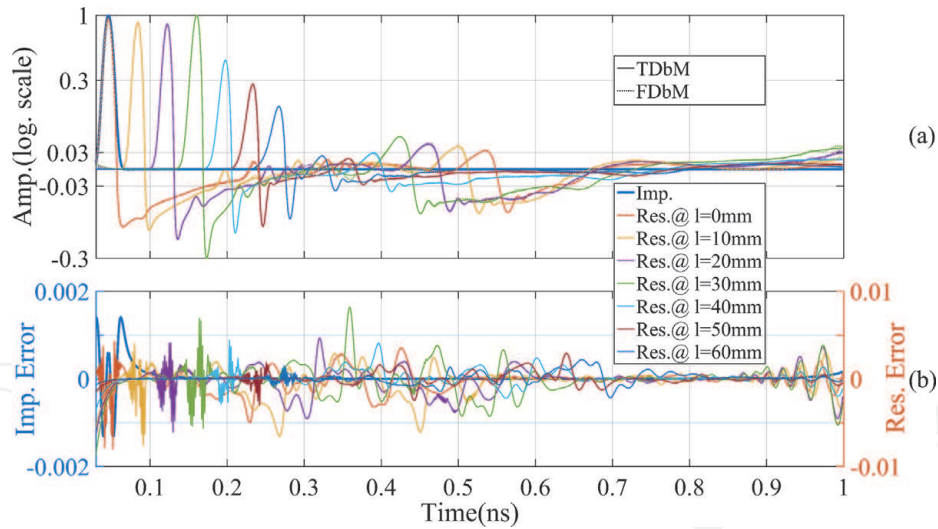


Figure 4.
The impulse and responses pairs with (a) TDbM and FDbM and (b) the corresponding errors.

superposition of different versions from the excitation source. This can be presented by a convolution of $x(t)$ and the impulse response of the propagation channel $h(t)$:

$$s(t) = x(t) * h(t). \quad (1)$$

In general, $h(t)$ can be continuous, but in the case of limited excitation signal BW and limits in space/time resolution of the EM simulation, it can be approximated by N discrete components (N can be large):

$$h(t) \approx \sum_{n=0}^{N-1} a_n \delta(t - \tau_n), \quad (2)$$

where δ is a Dirac function, and a_n and τ_n are the amplitude and delay time, respectively, of the n -th component.

The channel impulse response in the frequency domain is

$$H(f) \approx \sum_{n=0}^{N-1} a_n e^{-j2\pi f \tau_n}. \quad (3)$$

Considering noise (as white noise from EM solver errors) and with a sufficient SNR of the signals in the analysis band, an estimation of $H(f)$ can be implemented as

$$\hat{H}(f) = \frac{\hat{S}(f)}{X(f)} = H(f) + w'(f), \quad (4)$$

where $X(f)$ is the Fourier transform of $x(t)$, $\hat{S}(f)$ is the Fourier transform of $s(t)$ with the noise and $w'(f)$ is considered as the corresponding white noise in the frequency domain.

Thus,

$$\hat{H}(f) = \sum_{n=0}^{N-1} a_n e^{-j2\pi f \tau_n} + w(f), \quad (5)$$

where $w(f)$ is the total noise including the error of approximation in Eq. (3). In Eq. (5), $\hat{H}(f)$ can be considered as a harmonic model [15, 17], and τ_n are parameters needed to be estimated.

The MUSIC algorithm is applied to solve this problem in this work. $\hat{H}(f)$ is sampled with N_s samples and a frequency step of Δf in the frequency domain:

$$\begin{aligned}\hat{H}[k] &= \sum_{n=0}^{N-1} a_n e^{-j2\pi(k\Delta f)\tau_n} + w[k], k = 0, 1, \dots, N_s - 1 \\ w[k] &= w(k\Delta f).\end{aligned}\quad (6)$$

The matrix form of $\hat{H}[k]$ is

$$\hat{\mathbf{H}} = \mathbf{V}\mathbf{a} + \mathbf{w}, \quad (7)$$

where

$$\begin{aligned}\hat{\mathbf{H}} &= [\hat{H}[0] \hat{H}[1] \dots \hat{H}[N_s - 1]]^T \\ \mathbf{V} &= [\mathbf{v}(\tau_0) \mathbf{v}(\tau_1) \dots \mathbf{v}(\tau_{N-1})] \\ \mathbf{v}(\tau_n) &= [1 \ e^{-j2\pi((1)\Delta f)\tau_n} \dots e^{-j2\pi((N_s-1)\Delta f)\tau_n}]^T \\ \mathbf{a} &= [a_0 a_1 \dots a_{N-1}]^T \\ \mathbf{w} &= [w[0] w[1] \dots w[N_s - 1]]^T,\end{aligned}\quad (8)$$

T is a transpose of a vector.

The analysis band limitation is implemented by a rectangular window:

$$\begin{aligned}\hat{H}[k] &= u[k] \left(\sum_{n=0}^{N-1} a_n e^{-j2\pi(k\Delta f)\tau_n} + w[k] \right), k = 0, 1, \dots, N_s - 1 \\ u[k] &= \begin{cases} 1 & \text{if } F_{cL} \leq k\Delta f \leq F_{cH} \\ 0 & \text{otherwise,} \end{cases}\end{aligned}\quad (9)$$

where F_{cL} and F_{cH} are the lower and upper frequency bounds of the analysis band, respectively.

A Toeplitz data matrix \mathbf{Z} is established from $\hat{\mathbf{H}}$ array with a dimension factor D chosen as $D \geq N_0$, where $N_0 \leq N$ is the size of the signal subspace chosen in the analysis:

$$\mathbf{Z} = \begin{bmatrix} \hat{H}[D] & \dots & \hat{H}[0] \\ \vdots & \ddots & \vdots \\ \hat{H}[N_s - 1 - D] & \dots & \hat{H}[D] \\ \vdots & \ddots & \vdots \\ \hat{H}[N_s - 1] & \dots & \hat{H}[N_s - 1 - D] \\ \hat{H}^*[0] & \dots & \hat{H}^*[D] \\ \vdots & \ddots & \vdots \\ \hat{H}^*[D] & \dots & \hat{H}^*[N_s - 1 - D] \\ \vdots & \ddots & \vdots \\ \hat{H}^*[N_s - 1 - D] & \dots & \hat{H}^*[N_s - 1] \end{bmatrix}^{\mathcal{H}} \quad (10)$$

where \mathcal{H} is a Hermitian matrix transpose.

A covariance matrix \mathbf{R} is calculated based on this \mathbf{Z} matrix:

$$\mathbf{R} = \mathbf{Z}\mathbf{Z}^H. \quad (11)$$

With the \mathbf{R} covariance matrix, eigen decomposition is implemented and the signal and noise subspaces are separated [18]:

$$\mathbf{R} = \sum_{i=1}^{D+1} \lambda_i \boldsymbol{\psi}_i \boldsymbol{\psi}_i^H, \quad (12)$$

where λ_i and $\boldsymbol{\psi}_i$ are eigenvalues and eigenvectors, respectively. The ToA parameters can be estimated based on the peak positions of the MUSIC spectrum:

$$P(\tau) = \frac{1}{\|\boldsymbol{\Phi}^H \mathbf{e}(\tau)\|^2}, \quad (13)$$

where $\boldsymbol{\Phi} = [\boldsymbol{\psi}_{N_0+1} \boldsymbol{\psi}_{N_0+2} \dots \boldsymbol{\psi}_{D+1}]$ spans the noise subspace, and $\mathbf{e}(\tau) = [1e^{j2\pi(1)\tau/N_s} \dots e^{j2\pi(D)\tau/N_s}]^T$ is a steering vector [19].

This MUSIC algorithm is applied to directly analyze the observed signals (curve normal components of the E-field vectors at the points a distance l along an edge of a slot line structure as presented in **Figure 5(b)**). The analysis is implemented in the cases of $N_0 = 1$ and $N_0 = 500$.

- Analysis of expected single component $N_0 = 1$

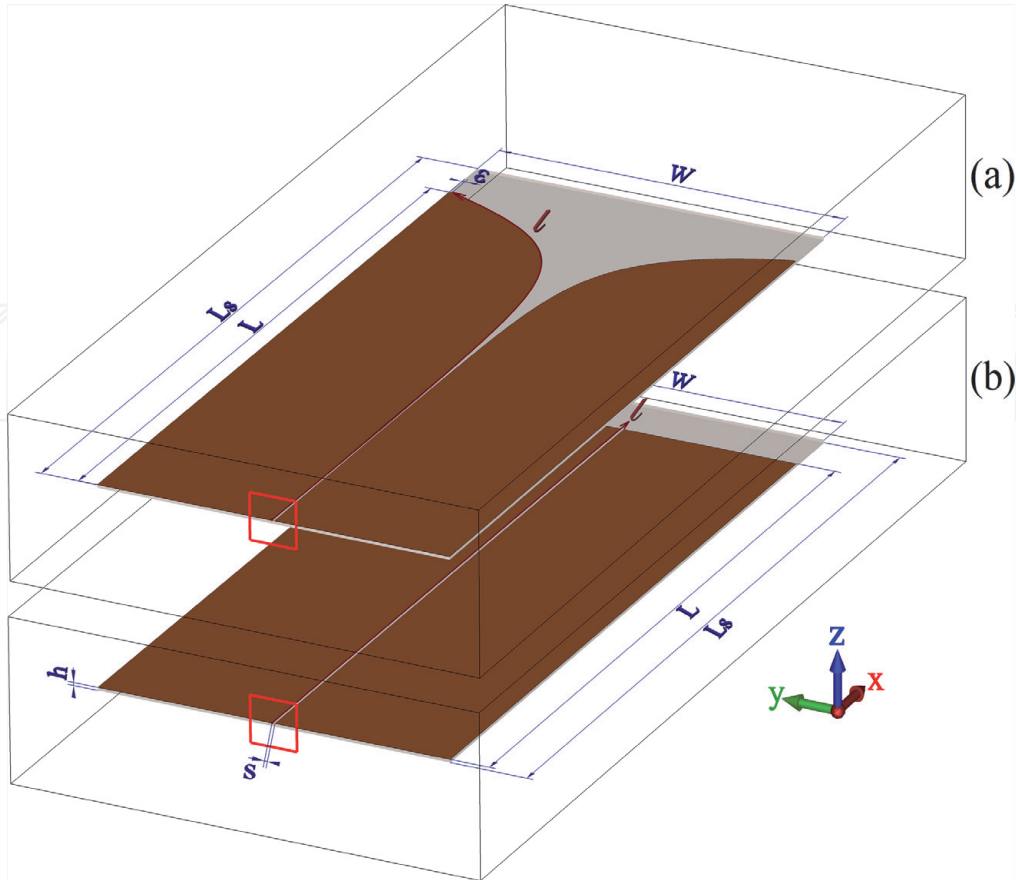


Figure 5.
 The structural models with excitation ports of (a) a Vivaldi antenna and (b) a slot line.

In the case of $N_0 = 1$, only one component in the signal subspace is expected. This corresponds to the most dominant component or cluster of the observed signal, and other components are considered as noise. The peak of the MUSIC spectrum is expected to indicate the ToA or time delay of this component or cluster.

MUSIC parameters are set as $N_0 = 1$; $D = 35$; $N_s = 1,250$; and $dt = 1$ ps in this analysis. The analysis is implemented in different bands of F_{cL} and F_{cH} . The response signals with the same bands limited by the Gaussian windows are calculated based on FDbM as the reference signals. **Figures 6** and 7 show the results of estimated ToAs and propagation velocities based on the response signals and the MUSIC spectra.

Figure 6 shows that the FDbM response signal shape changes with increasing l . The signal part to the left of the peak is getting wider than the part to the right of the peak, which tends to increase in negative potential. This denotes a left-shifting tendency in the FDbM response peaks versus distance l . Thus, the estimated ToAs based on the FDbM response peaks tend to shrink with distance l , while the peak positions of the MUSIC spectra increase regularly with l . In **Figure 7**, the feature can

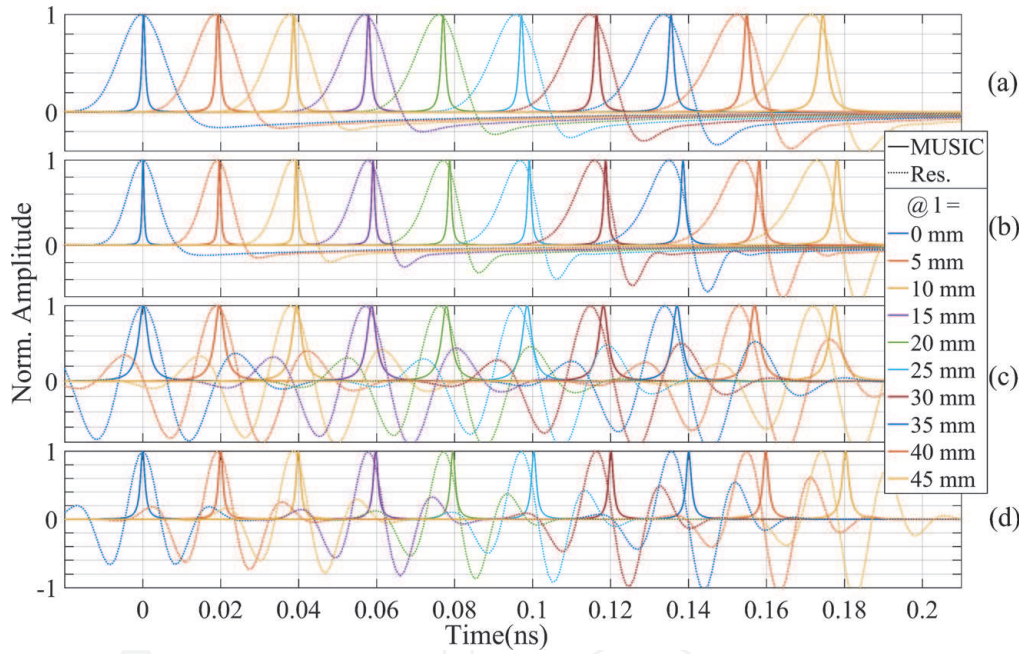


Figure 6. The MUSIC spectra and FDbM impulse response signals at the points along the slot line edge with analysis bands of (a) 0–60, (b) 0–90, (c) 20–60, and (d) 20–90 GHz.

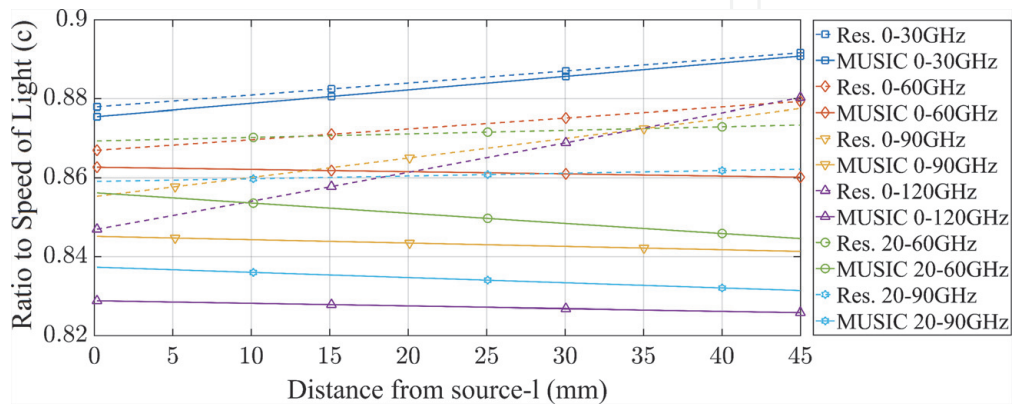


Figure 7. The estimated propagation velocities based on the FDbM response signal peaks and the MUSIC spectra in different analysis bands along the slot line edge.

be seen more clearly with the estimated propagation velocities. The estimated velocities based on the response peaks are faster than those based on MUSIC, and the difference increases with an increase in l , with an exception in the low-frequency band case (0–30 GHz), where the two methods show similar results. Furthermore, the estimated results based on MUSIC show reasonably constant velocities, independent of l , especially in wideband cases.

- Analysis of multi-components $N_0 = 500$

The analysis is observed at a point $l = 30 \text{ mm}$ on the slot line edge with a parameter set of $N_0 = 500$; $D = 738$; $N_s = 1,250$; and $dt = 1 \text{ ps}$ and an analysis band of 0–90 GHz. The dimension factor D equals 738 to ensure that a full slide over the samples generates the \mathbf{Z} matrix with a size of $738 \times 1,024$, and matrix columns contain all of the frequency components of the analysis band without redundancy. This ensures to capture adequately signal frequency information. In **Figure 8**, besides the MUSIC spectra, FDbM impulse response signals with a Gaussian window and a rectangular window to limit frequency in the same analysis band of 0–90 GHz are also calculated and presented.

With the larger N_0 in this analysis, the MUSIC spectrum shows synchronicity with the FDbM impulse response signals (limited by rectangular window); as seen in **Figure 8**, the spectrum is also eliminated at nulls of the response signal. This shows that accuracy of the estimation of the dominant component ToAs can be reduced at proximity of the zero crossings in the impulse response signals. In the case of $N_0 = 1$, this effect cannot be observed. Another observable feature in this analysis is that the variability in the MUSIC spectrum magnitude is not following the trend of the component or cluster magnitude of the corresponding response signal. Thus, the magnitude estimation for the separate components or clusters needs additional information other than the MUSIC spectrum.

3. Near-field propagation analysis for Vivaldi antenna design

3.1 Simulation structures and conditions

The near-field propagation analysis is implemented on the slot line and Vivaldi structures, as shown in **Figure 5**. A Rogers RT5880 ($\epsilon_r = 2.2$ and $\tan \delta = 0.0009$ at 10 GHz) dielectric substrate of width W , length L_s and thickness h ($-h \leq z \leq 0$) is used for the two structures. The metallic objects of the structures are built on the copper layer with a thickness of θ ($0 \leq z \leq \theta$).

The open-ended slot line consists of two copper patches with length L separated by a slot of width s . The symmetrical Vivaldi slot is built based on an exponential function:

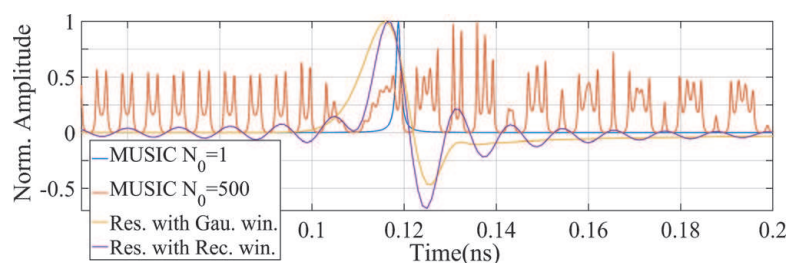


Figure 8.
 The MUSIC spectra and FDbM response signals at a point $l = 30 \text{ mm}$ along the slot line edge.

$$y = a(e^{px} - 1) + \frac{s}{2}, \quad 0 \leq x \leq L, \tag{14}$$

where a is a y -axis scale factor, and

$$a = \frac{\left(\frac{W}{2} - \frac{s}{2}\right) - \varepsilon}{e^{pL} - 1}, \tag{15}$$

where ε is the end segment width of the Vivaldi patch. The limits of the x variable and the y curve function are in the ranges of $0 \leq x \leq L$ and $\frac{s}{2} \leq y \leq \frac{W}{2} - \varepsilon$. **Table 2** shows the parameters of these structures.

The EM simulations were implemented in time domain with an open boundary condition. The distances from the structures to most of the boundaries are 5 mm, except at the radiation aperture boundary x_{max} , where the distance is 15 mm. Thus, the simulation volume is $85 \times 40 \times 10.265 \text{ mm}^3$. Differential waveguide ports with size of $4 \times 4 \text{ mm}^2$ ($x = 0, -2 \text{ mm} \leq y \leq 2 \text{ mm}, -2 \text{ mm} \leq z \leq 2 \text{ mm}$) excite these two structures, shown as red squares in **Figure 5**. An FMCW signal covering a band of 0–210 GHz and lasting 0.5 ns is the time-domain excitation signal. The observed signals are sampled at rate of 1 THz, and the sampled period is 1.25 ns.

3.2 Propagation analysis on the conducting plane

The $z = \theta$ plane contains the most valuable field data because it includes the top conducting surface of the antenna structure. In this plane, the FDbM impulse response analysis with Gaussian windows for frequency limiting is implemented for all of the observed signals in different bands. The complex field data are postprocessed and presented in different forms, and the field vector magnitude quantities are normalized according to the maximum corresponding field vector magnitude at the excitation port position ($x = 0, -\frac{s}{2} \leq y \leq \frac{s}{2}, z = \theta$).

3.2.1 Space distribution of field intensity

The intensity distributions are examined based on the maximum (over time) of the impulse responses of EM field vector magnitudes in the two analysis bands as shown in **Figure 9**. Noticeably, the strongest EM field intensities distribute along the slot line and Vivaldi slot, especially at the slot conduction edges. **Figure 9(b)** and **(c)** shows that because of the discontinuity in the structure of the reconstructed

Parameters	Slot line	Vivaldi antenna
L_s (mm)	65	65
L (mm)	60	60
W (mm)	30	30
s (mm)	0.25	0.25
h (mm)	0.25	0.25
θ (mm)	0.017	0.017
ε (mm)	—	0.25
p	0	0.2

Table 2.
Parameters of the slot line and Vivaldi antenna.

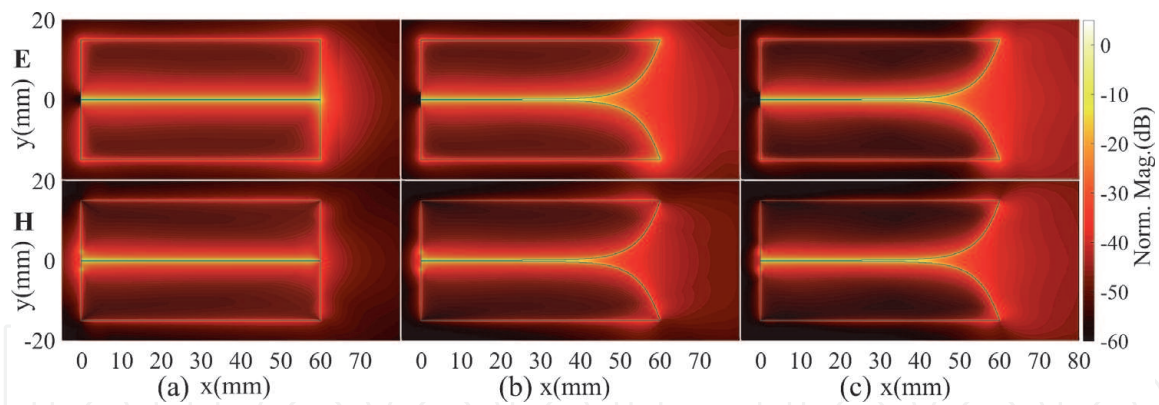


Figure 9.
 The maximum EM field vector magnitudes on the conducting plane of (a) a slot line and (b) and (c) a Vivaldi antenna in the analysis bands of (a) and (b) 0–30 GHz and (c) 0–60 GHz.

meshed Vivaldi slot, as mentioned in the Section 2.1.1, at these discontinuous locations, there are abrupt changes in the spatial distribution of field intensities. This is an expression of scattering phenomena in the propagation along the tapered structure of the Vivaldi slot.

These plots also reveal other features of the propagation, for example while the E-field intensity increases at the endpoints ($x = 60$ mm) of the slot line and Vivaldi slot, the H-field intensity reduces at these endpoints. The dielectric material transition from RT5880 to vacuum at the substrate edge ($x = 65$ mm) in the radiating aperture region leads to a small abrupt in the space distribution of the E-field intensity at the substrate edge. At the excitation port location, because of the limit in port width in the y direction, the H vectors change direction and their distribution is abrupt around the port edges ($x = 0, y = \pm 2$ mm). This leads to EM energy of the excitation source being dispersed into multiple directions other than $+x$, as per the port mode definition, and the port edges act like scattering sources.

3.2.2 Space distribution of first-ToA clusters and MUSIC spectra

At each point in space, the impulse response analysis result is a time distribution of clusters, and this distribution reveals propagation path information such as the number of paths, time delay, and attenuation characteristic. If the time distribution of a certain cluster can be identified for each point in space, then the space distribution information of this cluster is determined. This information reveals the effects of the structure's spatial characteristics on the cluster's propagation.

In propagation characterization, the most important cluster is the earliest- or first-ToA cluster. This cluster is formed by the propagating EM energy flows from the source over the shortest path with the fastest velocity. In this analysis, the ToA of the first cluster of the EM field vector magnitudes is estimated for each point in the conducting plane based on a local peak-finding algorithm. Direction and magnitude information of the field vectors corresponding to the first clusters is derived as illustrated in **Figures 10** and **11**. These results reveal how the first clusters of EM fields depend on material and spatial characteristics of the structure. **Figure 12** presents the space distribution of first-cluster ToAs or propagation times from the source. ToA contour lines play the role of two-dimensional wavefront and present visually the effects of the material and spatial characteristics of the structure on the clusters' propagations.

However, due to spreading of the analysis impulse in time and the overlapping of multiple EM flows, the total response signals can be canceled, flat or not distinguishable as separate clusters. In this case, ToA of the clusters cannot be estimated

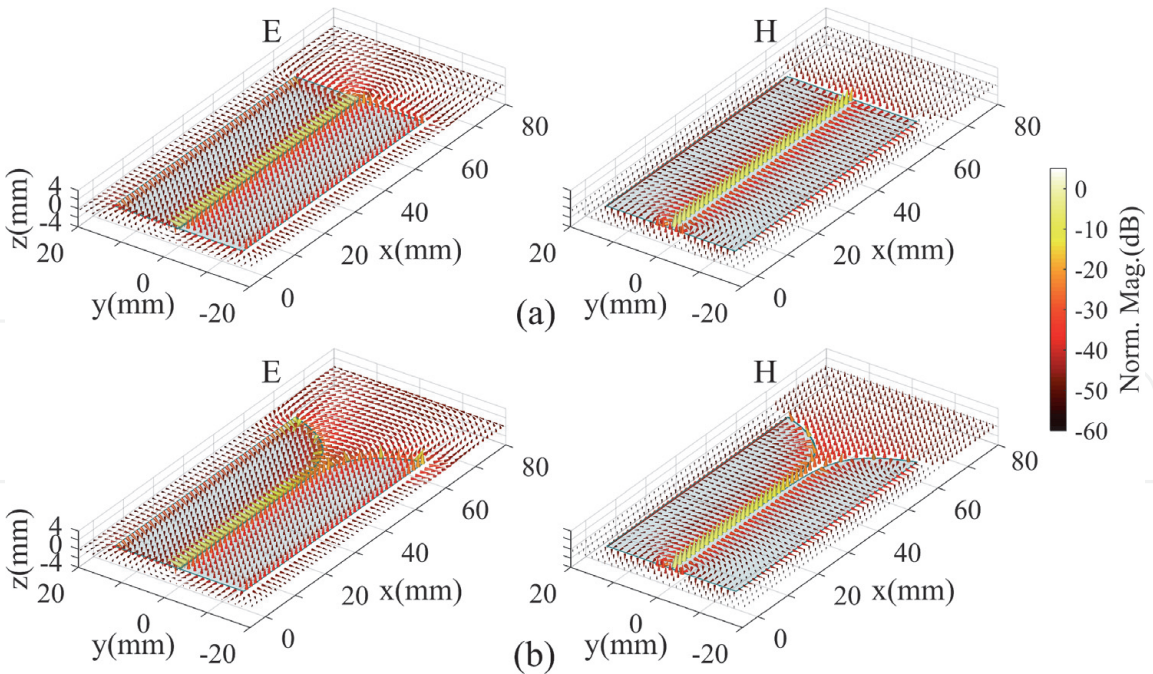


Figure 10.
The EM field vectors at the time of the first peaks on the conducting plane of (a) a slot line and (b) a Vivaldi antenna in the analysis bands of 0–30 GHz.

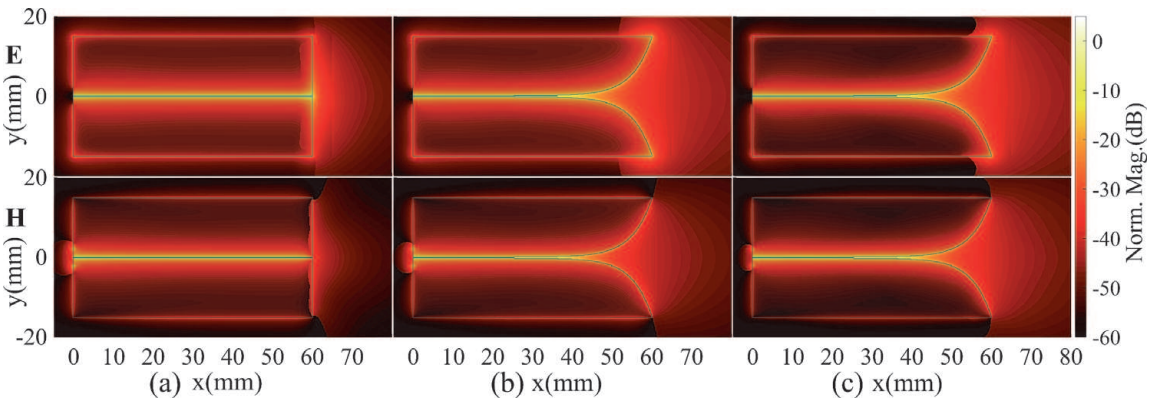


Figure 11.
The first-peak EM field vector magnitudes on the conducting plane of (a) a slot line and (b) and (c) a Vivaldi antenna in the analysis bands of (a) and (b) 0–30 GHz and (c) 0–60 GHz.

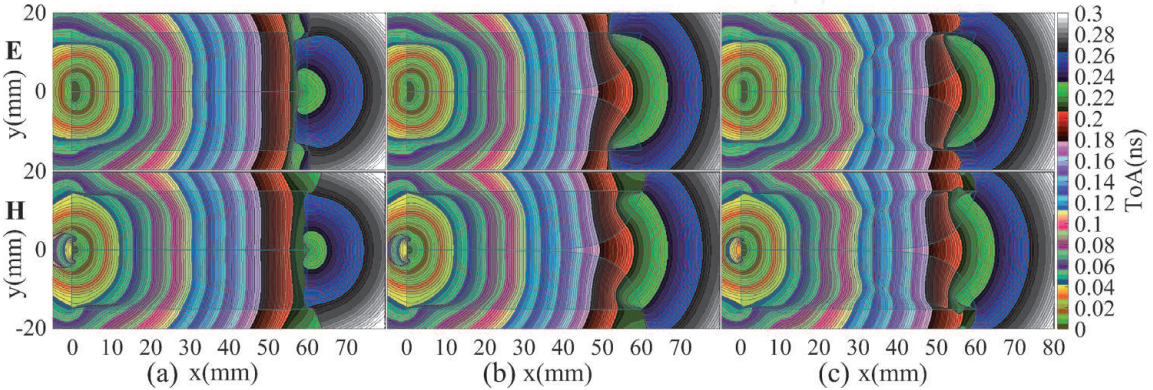


Figure 12.
The ToAs of the first clusters based on the first peaks of the EM field vector magnitudes on the conducting plane of (a) a slot line and (b) and (c) a Vivaldi antenna in the analysis bands of (a) and (b) 0–30 GHz and (c) 0–60 GHz.

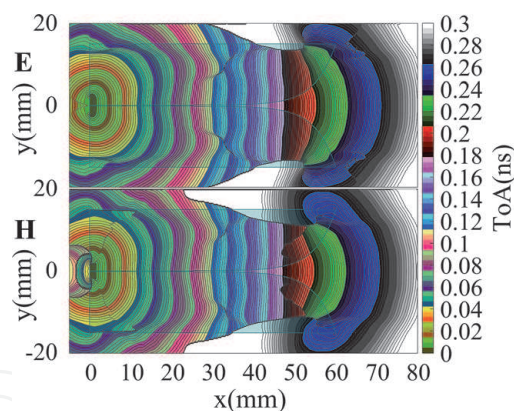


Figure 13.
 The ToAs based on the MUSIC spectra of EM field vectors on the conducting plane of a Vivaldi antenna in the analysis band of 0–60 GHz.

exactly, or the clusters cannot be distinguished in the time domain, and this can lead to significant estimation errors in the analysis results.

As described in Section 2.2.2, the MUSIC algorithm is used in this analysis for estimation of the ToA. The results of estimated ToAs are shown **Figure 13** based on the peaks of three MUSIC spectrum components summation of EM field vectors in the analysis band of 0–60 GHz and with MUSIC parameters $N_0 = 1$ and $D = 35$. Instead of presenting the ToA of the first cluster as the FDbM impulse response analysis, the result based on MUSIC spectra presents ToAs of the dominant component of the cluster with a certain correlation with the impulse. The comparison between **Figures 12(c)** and **13** shows that some dominant components are estimated by the MUSIC algorithm emerge in some regions, and their MUSIC ToAs are later than the FDbM impulse response ToAs. For example, at the lateral edges of the antenna, there are the scattered components from the Vivaldi endpoints, and these components cannot be shown in **Figure 12(c)** due to domination of the first clusters.

3.3 Propagation analysis on the edge of the slots

In this section, detailed near-field examinations of the slot line and Vivaldi slot conducting edge propagation are made along the l -axes from the sources as illustrated in **Figure 5**.

3.3.1 Field intensity on the edges

The stepped or staircase meshed structure of the Vivaldi antenna is different from the constant distance between the two parallel slot edges of the slot line. This structural feature is the cause of abrupt changes in intensity of the EM responses at transition positions along the Vivaldi edges as seen in **Figures 9** and **11**. In this section, this is investigated thoroughly based on the first-peak field vector magnitude analysis versus the distance from source l . The field vector magnitudes are normalized according to the first-peak vector magnitude of the corresponding field source.

Figure 14 shows that the propagations on the slot line and the Vivaldi slot are similar in the first segment ($0 \leq l \leq 24$ mm). The transition positions on the Vivaldi edge lead to scattering at these points, and both the E and H vectors magnitudes increase abruptly after the transition points. However, because of expansion in slot width after each transition position and this scattering, the concentration of EM energy flows on the edge in the $+l$ direction is reduced after each transition position. Faster reduction of the magnitudes versus l after each transition position

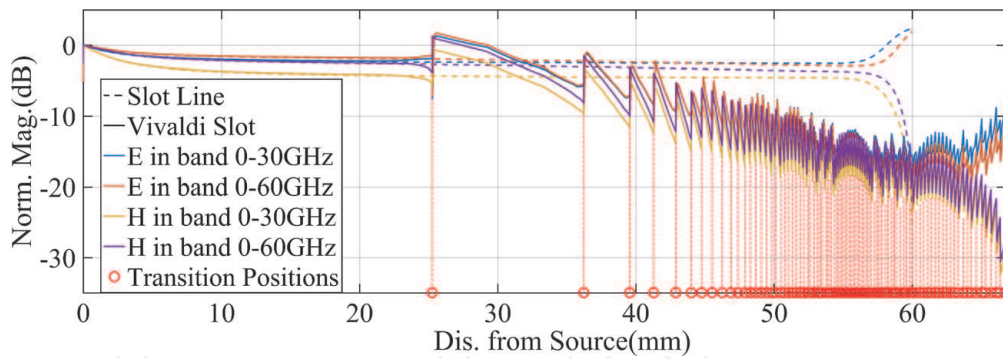


Figure 14. The first peak of the EM field vector magnitudes on the edge of the slot line and Vivaldi slot versus the distance from source l .

demonstrates this spreading. Superposition between the incident first cluster from the source and the dominant scattering/reflecting cluster from the endpoint of the slot edges increases the E field vector magnitude and reduces the H field vector magnitude.

3.3.2 Propagation progress along the edges

To observe the propagation progress/process along the edges, the EM response signals versus time and versus distance l from the source at consecutive points along the edges are examined. Structural effects on the signals and/or general propagation process are analyzed based on the changes in cluster shape or emergence of scattering signals in time domain versus l . Specifically, the analysis quantities are the EM vector magnitudes and dominant vector components along the curves l . An adequate information about the field intensity can be provided by the EM vector magnitudes, while a change of sign in the dominant vector components can indicate a reversal in vector direction. To eliminate the abrupt difference in intensity at transition points along the edges, the analysis quantities are normalized according to peaks of the first cluster. The normalized signals on the slot line and Vivaldi slot versus time and l are shown in **Figures 15** and **16**. These show that the signal tendencies can be seen clearly with increasing of l .

- Slot line

Some key features of the propagation process can be disclosed from **Figure 15** with/without a reference to the original magnitudes in **Figure 14**. Specifically, the main cluster transferring from the source through the slot line path in the $+l$ direction corresponds to the A cluster/ledge in **Figure 15(a)**. In the propagation process, time response of the impulse signal to the slot line structure forms the B or B' cluster. In detail in **Figure 15(b)**, negative potential of the B cluster shows that the vector direction corresponding to the B cluster is opposite to that of the A cluster. The A (and B) clusters reflected at the slot line open end form the C cluster propagating back to the source, and the C-cluster reflection at the source position creates the E cluster. A part of scattering energy at the slot line open end of the A (and B) cluster forms EM flow traveling along the end edge ($x = 60$ mm, in the $+y/ -y$ direction); this is scattered again at the lateral edge, and a part of scattering energy propagates back to the open-end position and the source, forming the D cluster.

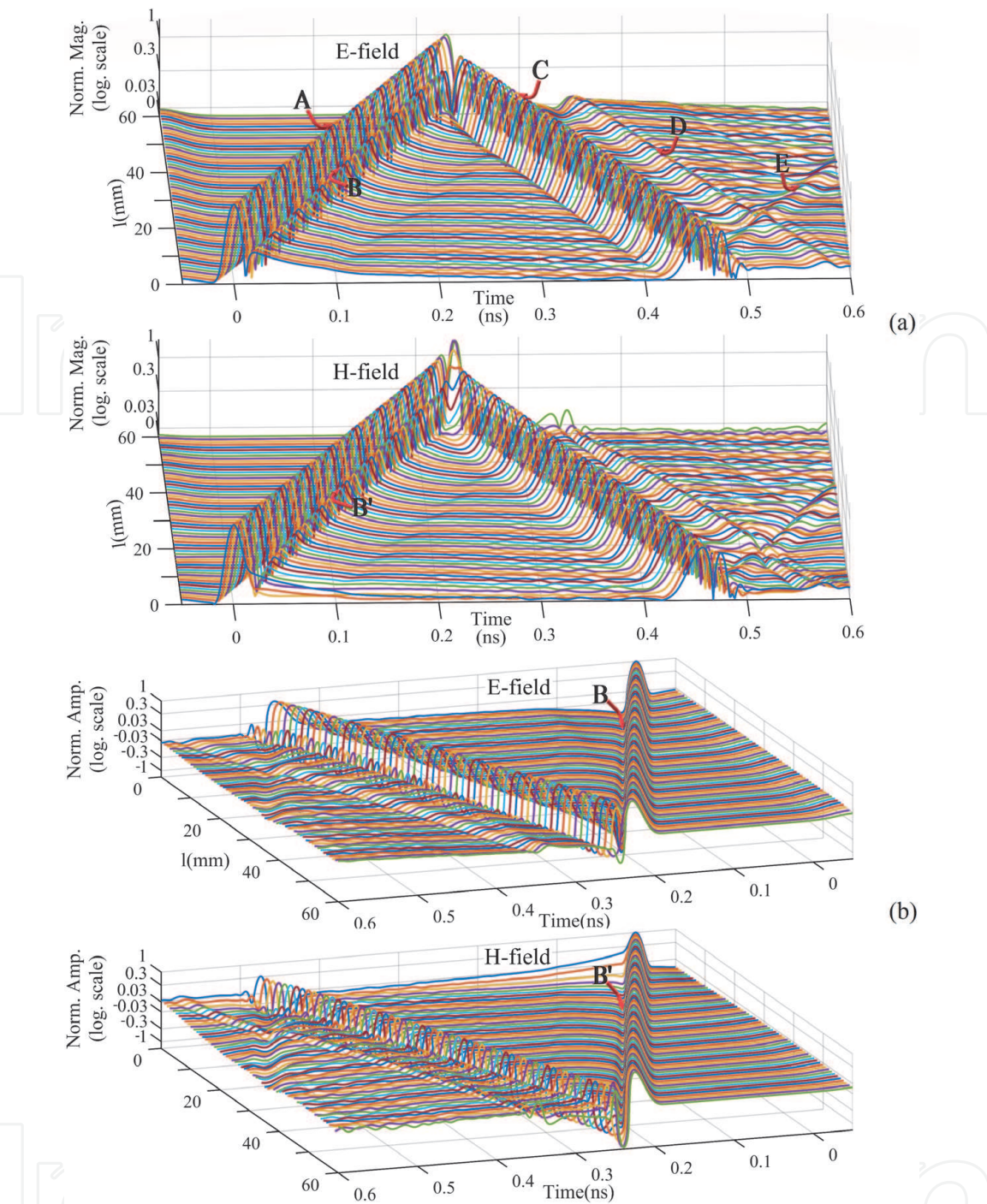


Figure 15. (a) The vector magnitude signals and (b) the curve normal/surface normal vector component signals of the EM fields on the edge of the slot line versus time and versus distance from source l in the analysis band of 0–60 GHz.

- Vivaldi slot

Besides the A, B and C clusters being similar to the slot line edge response, along the Vivaldi edge, the first-order scattering components affect significantly to the propagation process. Particularly, scattering of the A and B clusters at the transition positions forms a series of clusters, such as the F and G clusters illustrated in **Figure 16**. Additionally, the C cluster is also scattered at these transition positions when traveling in the $-l$ direction. This disperses the EM energy and leads to a reduction in C and E clusters' intensities when compared with the A cluster. The scattering at the transition points and Vivaldi curve deflection in the $+y/-y$ directions also affect the A cluster. The cluster width increases and its peaks tend to earlier zones of ToA with increasing of l .

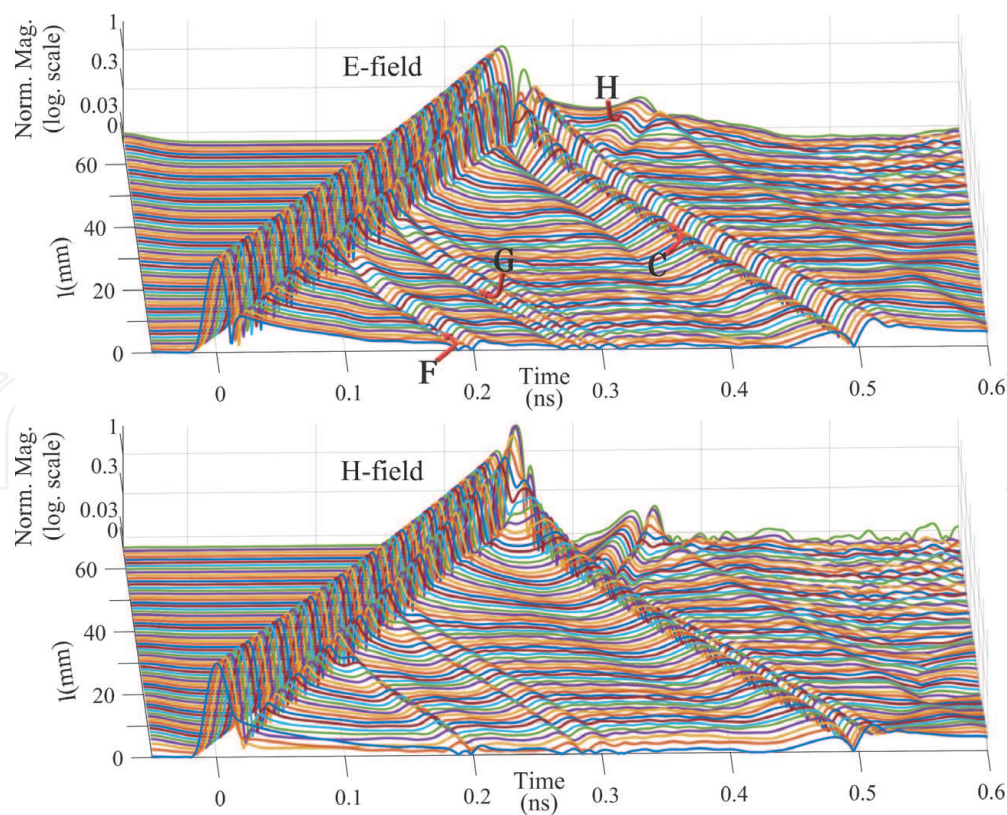


Figure 16.
The vector magnitude signals of the EM fields on the edge of the Vivaldi slot versus time and versus distance from source l in the analysis band of 0–60 GHz.

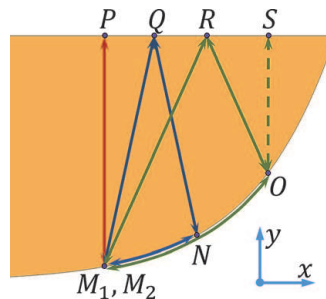


Figure 17.
Examples of paths of second- and third-order scattering components on the end of the Vivaldi taper.

The H cluster in **Figure 16** reveals a noticeable feature in the Vivaldi slot propagation process. The accumulation and combination of second- and higher-order scattering components arriving from continuous spatial sections form the H cluster. Examples of the spatial sections creating second- and/or third-order scattering components are illustrated in **Figure 17**. Assume that point M_1 is the starting point for high-order scattering paths from the A cluster, and M_2 , having the same position as M_1 , is the end point for these high-order scattering paths and for H cluster examination. A major proportion of the H cluster is contributed from second-order scattering components, such as components propagating over the M_1PM_2 , M_1NQM_2 and M_1ORM_2 paths, in which M_1 (in M_1PM_2 path), N and O are the first-order scattering points of the A cluster; and P , Q and R are the second-order scattering points. Third-order scattering components also contribute to intensity of the H cluster, such as M_1QNM_2 and M_1ROM_2 paths, in which M_1 is the first-order scattering point, Q and R are the second-order scattering points, and

N and O are the third-order scattering points. M_1OSOM_2 is another third-order path, in which O is the first- and third-order scattering point and S is the second-order scattering point.

3.4 Analyses summary

The plots of the maximum and first EM cluster intensity distributions in **Figures 9(b) and (c), 10(b), 11(b) and (c), and 14** reveal important regions/points in the Vivaldi structure with high-density EM flow and associated first-order scattering, which contribute to the main EM energy proportion of the total radiation. As seen in **Figure 14**, the scattering degree at the transition positions can be evaluated primarily by 3–6.5 dB abrupt changes in magnitude. This scattering degree can also be assessed based on the cluster intensities in **Figure 16** and with a reference to the first-cluster intensities in **Figure 14**. The magnitude reduction along the Vivaldi edges in **Figure 14** indicates the EM energy transfer out of the antenna conducting element into the free space.

The propagation of EM first clusters in the structures can be observed and quantified in terms of field vector direction and magnitude of first clusters based on **Figures 10 and 11** and ToA of first clusters based on **Figures 12 or 13**. All three space distributions of field vector direction, magnitude, and ToA of first clusters in these figures provide adequate information of propagation of EM first clusters in the observed space, and the important features of the propagation can be recognized. For example, as seen in **Figures 10(b), 11 and 12(b) and (c)**, and also in **Figure 13**, the propagation process of first clusters on the metal plane of the Vivaldi antenna and the degree of local EM flows were revealed. These also revealed intensity of scattering fields at the antenna aperture, and geometric features of the field propagation were also revealed such as the flare effect of the EM flow propagating away from the Vivaldi patches at the aperture. This is a significant factor in the reduction of antenna directivity.

The propagation progress investigation on the main propagation path, such as the results shown in **Figures 15 and 16**, not only provides more details of propagation of the first clusters, but it also reveals formation of other clusters due to scattering at the detail elements of the structure. Additionally, features of the formed clusters are also observed and evaluated. Based on these information, higher-order scattering components and corresponding propagation paths can be recognized or inferred. For example, the H cluster formation in **Figure 16** reveals the higher-order scattering at the lateral edge and the Vivaldi edge, as illustrated in **Figure 17**. The scattering on the lateral edge causes partial radiation in unwanted directions and reduces the total directional characteristic.

Based on this knowledge about mechanism in propagation and radiation on the structure and influences of the structural detail elements, the solutions can be proposed to increase the advantage features and to reduce the disadvantage features of the propagation to improve the total responses of the antenna. For example, methods to reduce the flare effect at the Vivaldi antenna aperture are adjustment of the Vivaldi p-factor, introduction of a core element, conversion of the antenna into a double-slot structure in [11], and insertion of a material structure at the antenna aperture to adjust the directions and/or velocities of the local EM flows. The estimated results for magnitude, ToA, velocity, and direction of EM flows propagation at specific regions at conducting edges and/or in the radiating aperture support the effectiveness of these refined adjustment methods. Another example solution for the higher-order scattering on the lateral edge was proposed. By addition of 45° ripples on the lateral edge in [11], a part of this energy is redirected into the antenna end-fire direction. This improves the antenna gain in a certain frequency band.

It also reduces the EM energy portion coming back to the source, thereby improving the S_{11} characteristic.

4. Conclusions

In the perspective of considering propagation to be the fundamental basic of dynamic electromagnetic phenomena, the comprehensive space/time/frequency analysis method of near-field propagation was proposed. Based on this, detailed knowledge of behavior and physical effects of the structures and/or objects to dynamic electromagnetics was revealed, and these also are basic for the refined optimization in design. With the fundamental basic and generality, applicability of this analysis technique is not limited to the example cases of this work. Besides Vivaldi antennas, this analysis technique can be applied for the analysis, designs, and optimization of any sort of traveling-wave antennas or transmission structures.

Author details


Ha Hoang^{1,2}

1 Department of Telecommunications Engineering, Faculty of Electrical and Electronics Engineering, Ho Chi Minh City University of Technology (HCMUT), Ho Chi Minh City, Vietnam

2 Vietnam National University Ho Chi Minh City, Ho Chi Minh City, Vietnam

*Address all correspondence to: hahoang@hcmut.edu.vn; hmanhha@gmail.com

IntechOpen

© 2021 The Author(s). Licensee IntechOpen. This chapter is distributed under the terms of the Creative Commons Attribution License (<http://creativecommons.org/licenses/by/3.0>), which permits unrestricted use, distribution, and reproduction in any medium, provided the original work is properly cited. 

References

- [1] Balanis CA. *Modern Antenna Handbook*, pp. 3–56, 263–367. New York, N.Y: Wiley; 2008
- [2] Gibson PJ. The Vivaldi aerial. In: *Proc. 9th European Microwave Conf.* Brighton, U.K; Sept. 1979. pp. 101–105
- [3] Janaswamy R, Schaubert D. Analysis of the tapered slot antenna. *IEEE Transactions on Antennas and Propagation*. 1987;**35**(9):1058–1065
- [4] Oraizi H, Jam S. Optimum design of tapered slot antenna profile. *IEEE Transactions on Antennas and Propagation*. 2003;**51**(8):1987–1995
- [5] Stockbroeckx B, Vander Vorst A. Electromagnetic modes in conical transmission lines with application to the linearly tapered slot antenna. *IEEE Transactions on Antennas and Propagation*. 2000;**48**(3):447–455
- [6] Stockbroeckx B, Vander Vorst A. Copolar and cross-polar radiation of Vivaldi antenna on dielectric substrate. *IEEE Transactions on Antennas and Propagation*. 2000;**48**(1):19–25
- [7] Ergul O, Gurel L. *The Multilevel Fast Multipole Algorithm (MLFMA) for Solving Large-Scale Computational Electromagnetics Problems*. Hoboken, NJ: Wiley; 2014. p. 2
- [8] Biswas B, Ghatak R, Poddar DR. A fern fractal leaf inspired wideband antipodal Vivaldi antenna for microwave imaging system. *IEEE Transactions on Antennas and Propagation*. 2017;**65**(11):6126–6129
- [9] Bai J, Shi S, Prather DW. Modified compact antipodal Vivaldi antenna for 4–50-GHz UWB application. *IEEE Transactions on Microwave Theory and Techniques*. 2011;**59**(4):1051–1057
- [10] M. Abbak, M. N. Akinci, M. Çayören, and I. Akduman, “Experimental microwave imaging with a novel corrugated Vivaldi antenna.” *IEEE Transactions on Antennas and Propagation*. 2017;**65**(6):3302–3307
- [11] Hoang H, Yang K, John M, McEvoy P, Ammann MJ. Ka-band planar Vivaldi antenna with a core for high gain. *IET Microwaves, Antennas and Propagation*. 2019;**13**(6): 732–735
- [12] Nassar IT, Weller TM. A novel method for improving antipodal Vivaldi antenna performance. *IEEE Transactions on Antennas and Propagation*. 2015;**63**(7):3321–3324
- [13] Hoang H, John M, McEvoy P, Ammann MJ. Near-field propagation analysis for Vivaldi antenna design: Insight into the propagation process for optimizing the directivity, integrity of signal transmission, and efficiency. *IEEE Antennas and Propagation Magazine*. 2021;**63**(5):46–60
- [14] Ge F-X, Shen D, Peng Y, Li VOK. Super-resolution time delay estimation in multipath environments. *IEEE Transactions on Circuits and Systems I: Regular Papers*. 2007;**54**(9):1977–1986
- [15] Alsindi N, Li X, Pahlavan K. Analysis of time of arrival estimation using wideband measurements of indoor radio propagations. *IEEE Transactions on Instrumentation and Measurement*. 2007;**56**(5):1537–1545
- [16] Di Claudio ED, Parisi R, Jacovitti G. Space time MUSIC: Consistent signal subspace estimation for wideband sensor arrays. *IEEE Transactions on Signal Processing*. 2018;**66**(10): 2685–2699
- [17] Manolakis DG, Ingle VK, Kogon SM. *Statistical and Adaptive Signal Processing*, pp. 149–445, 478. New York: McGraw-Hill; 2000

[18] Fereidoony F, Sebt MA, Chamaani S, Mirtaheri SA. Model-based super-resolution time-delay estimation with sample rate consideration. *IET Signal Processing*. 2016;**10**(4):376-384

[19] Ge F-X, Shen D, Peng Y, Li VOK. Super-resolution time delay estimation in multipath environments. *IEEE Transactions on Circuits and Systems I: Regular Papers*. 2007;**54**(9):1977-1986